Ultramicroscopy 253 (2023) 113808

Contents lists available at ScienceDirect

Ultramicroscopy

journal homepage: www.elsevier.com/locate/ultramic

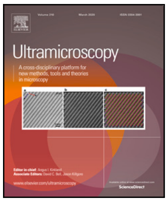

Quantitative electric field mapping between electrically biased needles by scanning transmission electron microscopy and electron holography

Jean Felix Dushimineza [a,b], Janghyun Jo [b], Rafal E. Dunin-Borkowski [b], Knut Müller-Caspary [a,b,*]

[a] *Department of Chemistry and Centre for NanoScience, Ludwig-Maximilians-Universität München, Butenandtstrasse 11, 81377 Munich, Germany*
[b] *Ernst Ruska-Centre for Microscopy and Spectroscopy with Electrons (ER-C), Forschungszentrum Jülich, 52425 Jülich, Germany*

ARTICLE INFO

Keywords:
First-moment STEM
4D-STEM
Off-axis electron holography
Electric field mapping
Perturbed reference wave effect
Finite-element analysis
Multislice

ABSTRACT

Stray electric fields in free space generated by two biased gold needles have been quantified in comprehensive finite-element (FE) simulations, accompanied by first moment (FM) scanning TEM (STEM) and electron holography (EH) experiments. The projected electrostatic potential and electric field have been derived numerically under geometrical variations of the needle setup. In contrast to the FE simulation, application of an analytical model based on line charges yields a qualitative understanding. By experimentally probing the electric field employing FM STEM and EH under alike conditions, a discrepancy of about 60% became apparent initially. However, the EH setup suggests the reconstructed phase to be significantly affected by the perturbed reference wave effect, opposite to STEM where the field-free reference was recorded subsequently with unbiased needles in which possibly remaining electrostatic influences are regarded as being minor. In that respect, the observed discrepancy between FM imaging and EH is resolved after including the long-range potential landscape from FE simulations into the phase of the reference wave in EH.

1. Introduction

Quantification of the charge distribution within matter and the corresponding electric field is indispensable for materials science as materials properties predominantly emerge from the electronic structure, such as ferroelectricity, polarisation-induced electric fields, or electric fields at pn-junctions. As the theoretical assessment of the charge distribution, e.g., via density functional theory, is limited in treating non-periodicity and structural inhomogeneity of solid-state materials compelling large-scale system calculations, experimental access to the electrostatic field or potential distribution is highly desirable. In particular, transmission electron microscopy (TEM) enables probing the electric field and potential by electron beam deflection and phase shift, synonymously.

In ferroelectrics, for example, the electric polarisation state is commonly investigated by TEM imaging of atomic displacements [1–4] and strain mapping using dark field electron holography [5,6]. Yet, quantification of intrinsic electric fields has been hindered due to the imprecise knowledge of the impacts of screening charges, defects and structural inhomogeneities. Methodologically, the measurement and quantification of polarisation-induced electric fields within matter via TEM can be crucially hampered by dynamical scattering and thickness effects [7]. A possible solution to mitigate such artefacts could be in-situ biasing of, e.g., ferroelectric thin films. Potentially, TEM data recorded at different voltages could be used to isolate the effect of polarisation-induced electric fields in a differential manner. Consequently, understanding the impact of the stray fields produced by the usually nanometre-sized electrodes is of central importance. In that respect, an obvious prerequisite is the quantifiability of the electric field distribution in free space produced by electrodes of known geometry without a specimen in between.

Promisingly, evaluation of stray electric fields emanating from a material's surface into vacuum is hardly affected by dynamical scattering. The absent atomic potentials, moreover, facilitates the evaluation of measurements since projection assumptions such as the phase object approximation (POA) or the weak phase object approximation (wPOA) appear applicable. Furthermore, stray electric fields can also be present without external bias, e.g. due to spontaneous polarisation in ferroelectrics, where surfaces with separated charges may strike vacuum. Measuring the resulting electric field spread in free space can then reveal first-hand information on the causative surface charge distribution [8]. Eventually, the surface charge is quantifiable without invasive transmission through the sample. Consequently, estimation of sample charging in general, e.g. induced by the electron beam itself, is experimentally approachable via stray electric fields. In addition,

---

[*] Corresponding author at: Department of Chemistry and Centre for NanoScience, Ludwig-Maximilians-Universität München, Butenandtstrasse 11, 81377 Munich, Germany.

E-mail address: k.mueller-caspary@cup.lmu.de (K. Müller-Caspary).

https://doi.org/10.1016/j.ultramic.2023.113808
Received 15 April 2023; Received in revised form 24 June 2023; Accepted 30 June 2023

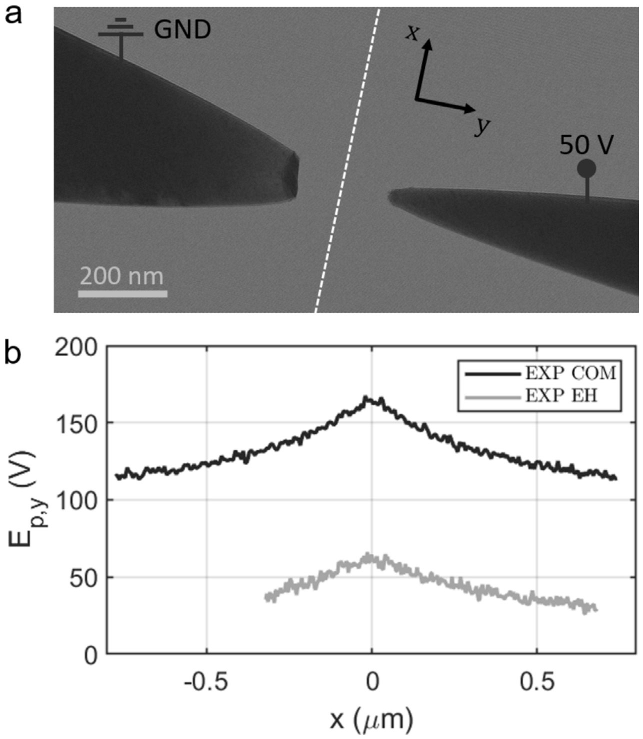

Fig. 1. (**a**) TEM image of experimental setup consisting of two opposing gold needles separated by a distance of 200 nm. Between the needles, a biasing voltage of 50 V is applied in which the needle at the left-hand side is set to ground. The needle setup was used for the EH measurements as well as for the COM measurements. (**b**) The y-component of the projected electric field $E_{p,y}$ is plotted along the dotted line in (a) for COM and EH, respectively.

interface properties of polar nanostructures can be investigated by making use of stray electric fields. As is well known, separated space charges across a pn-junction compel an embedded electric field. Once more, the emanating electric fields at the surface in vicinity of the pn-junction can be probed without electron-beam penetration of the sample and even increased via reverse biasing [9]. Hence, stray electric fields do not only play a crucial role in non-biasing experiments but also in *in-situ* switching experiments. Importantly, the biasing architecture itself may generate stray electric fields of the electrodes whose contribution has to be quantified to reassess the electric field distribution of interest due to the material response only, which requires comparison with theoretical models and simulations. This raises the question to which extent long-range electric fields perturb the electron waves in established approaches for electrical characterisation, namely electron holography [10,11] (EH) and centre of mass [12,13] (COM) or, equivalently, first moment (FM) scanning TEM (STEM).

In this work, long-range stray electric fields generated between two biased needles, as shown in Fig. 1a, serve as a model system to work out consistency between FM STEM and conventional off-axis EH regarding their capability to quantify electric fields in the absence of dynamical scattering. Recently, the conceptual differences between COM and EH have been elaborated theoretically and by considering the effect of dynamical scattering in crystals via simulations [14]. Here, on the occasion of experimentally observed discrepancies between COM and EH in the measured projected electric field depicted in Fig. 1b, the impact of methodological differences on long-range field measurements is elucidated. To this end, the fundamentals of both methods are briefly summarised at first, followed by simulations of the 3D electric field distributions within the biasing setup obtained by finite element [15] (FE) calculations which in turn are used as input to simulate the electron wave propagation and electron–optical phase shift for STEM and EH, respectively. Considerable attention is drawn to the impact of the perturbed reference wave in EH, which turns out to be significant for the present setup conditions and responsible for the discrepancy. Additionally, the results of the FE simulations are compared to an analytical model in which the 3D potential distribution is based on line charges [16]. Finally, FE simulations are combined with multi- and single slice electron scattering approaches to study the reliability of the projection assumption for fields with millimeter extension along the electron beam direction. Governing parameters such as the needle geometry, electron energy and STEM semi-convergence angle, are studied in detail as to their impact on the measured electric field. The paper closes with a comprehensive discussion.

2. Methods

2.1. Experimental setup

The electric field to be mapped is generated via two gold needles separated by 200 nm which have been electrically biased by applying a voltage of 50 V (Fig. 1). Both needles are placed onto a biasing TEM holder (Nanofactory STM-TEM) of which one is fixed at the holder end and the other one is clamped onto an opposing movable piezo tube. For the needle fabrication, a single gold wire is etched using an ElectroPointer with an HCl-ethanol solution resulting in two needles with narrowing tips.

The FM STEM data has been recorded at a FEI Titan G2 80-200 ChemiSTEM microscope operated at 200 kV with a semiconvergence angle of 4 mrad employing an EMPAD detector [17]. The EH measurement was performed on a FEI Titan G2 60-300 HOLO operated at 300 kV employing a K2 camera.

2.2. First-moment STEM

The FM method or also addressed as COM imaging method [12,13] enables electric field measurements in STEM mode via recording a full diffraction pattern at each position of the scanning probe. From a general viewpoint, the results of the COM measurement are determined by the three-dimensional distribution of the electrostatic potential $V(\vec{r}_\perp, z)$ within an interaction volume. Here, $\vec{r}_\perp = (x, y)$ denotes a two-dimensional vector perpendicular to the optical axis which runs along z. In STEM, a focused probe is scanned across the $\vec{r}_\perp$ plane on a raster with lateral positions $\vec{R}$. Assuming that the probe wave functions are identical for each scan position except for a translation, the incident electron wave can be parameterised by $\vec{R}$, i.e. $\Psi_{\mathrm{in}}(\vec{r}_\perp, \vec{R})$.

Interaction with $V(\vec{r}_\perp, z)$ leads to a real space exit wave function $\Psi_{\mathrm{ex}}(\vec{r}_\perp, \vec{R})$ for each scan position. In momentum-resolved STEM, the squared modulus of its Fourier transform

$$I(\vec{k}_\perp, \vec{R}) = |\Psi_{\mathrm{ex}}(\vec{k}_\perp, \vec{R})|^2 \tag{1}$$

yields the recorded diffraction pattern $I(\vec{k}_\perp, \vec{R})$ with two-dimensional reciprocal coordinates $\vec{k}_\perp$. The average momentum transferred to the incident STEM probe at scan position $\vec{R}$ is given by the first moment

$$\langle \vec{p}_\perp \rangle(\vec{R}) = \iint_{-\infty}^{\infty} I(\vec{k}_\perp, \vec{R}) \cdot \vec{k}_\perp \, d^2k_\perp \,, \tag{2}$$

being the quantum mechanical expectation value of the lateral momentum. Whereas Eq. (2) is exact also in the presence of multiple scattering, directly relating the measurement of $\langle \vec{p}_\perp \rangle$ to the projected electric field involves the assumption of single scattering. Identical expressions are obtained on the basis of Ehrenfest's theorem, or the phase object approximation [14] (POA). The methodological comparison with EH in the present study suggests using the POA, in which the exit wave is given by

$$\Psi_{\mathrm{ex}}(\vec{r}_\perp, \vec{R}) \approx \Psi_{\mathrm{in}}(\vec{r}_\perp, \vec{R}) \cdot e^{i\sigma V_{\mathrm{p}}(\vec{r}_\perp)} \quad , \tag{3}$$

with $V_\mathrm{p}(\vec{r}_\perp)$ the projected potential of the total interaction volume and σ the interaction constant. Calculating $\langle \vec{p}_\perp \rangle(\vec{R})$ from Eq. (3) yields

$$\langle \vec{p}_\perp \rangle(\vec{R}) \approx \frac{e}{v} \cdot \iint_{-\infty}^{\infty} I_\mathrm{in}(\vec{r}_\perp - \vec{R}) \cdot \vec{\nabla} V_p(\vec{r}_\perp)\, d^2 r_\perp \tag{4}$$

with I_in the intensity of the incident STEM probe, e the elementary charge and v the velocity of the electrons. Noticing Eq. (4) to be a cross-correlation, it can be brought to a compact form

$$\langle \vec{p}_\perp \rangle(\vec{R}) \approx \frac{e}{v} \cdot I_\mathrm{in} \otimes \vec{\nabla} V_p = -\frac{e}{v} \cdot I_\mathrm{in} \otimes \vec{E}_p \tag{5}$$

with the projected electric field $\vec{E}_p$. In case $\vec{E}_p(\vec{r}_\perp)$ does not vary significantly at the scale of the probe, and propagation effects can be neglected,

$$\langle \vec{p}_\perp \rangle(\vec{R}) \approx \frac{e}{v} \vec{\nabla} V_p = -\frac{e}{v} \cdot \vec{E}_p(\vec{R}) \quad . \tag{6}$$

Ultimately, the equivalency of Eqs. (2) and (4), (5), (6) reveals that, in POA, the projected electric field can be quantified in a momentum-resolved STEM experiment at a spatial resolution given by the STEM probe intensity.

A key requirement for an accurate measurement of $\vec{E}_p(\vec{R})$ via first moments is, according to the above derivation, $\langle \vec{p}_\perp \rangle(\vec{R}) = 0$ for $\vec{E}_p(\vec{R}) = 0$. Usually, a second measurement $\langle \vec{p}_\perp \rangle_0(\vec{R})$ is, therefore, performed subsequently without biasing the needles. Assuming that further charging of the surrounding and scan distortions are identical in that scan, subtraction from Eqs. (5), (6) yields the unperturbed result for the measurement of $\vec{E}_\mathrm{p}(\vec{R})$.

In general, the applicability of the POA implies a restriction to very thin specimens, because the atomic electric fields are strong enough to cause dynamical scattering effects become significant at thicknesses of a few nanometers. In the present case, the potential gradients are comparably small if the needles in Fig. 1 are biased to some tens of volts. However, we will show that the electric field may extend as long as millimeters along z direction, such that the impact of propagation effects and the direct applicability of Eqs. (4), (5), (6) will be explored below in a multislice study.

2.3. Electric field mapping in off-axis EH

In conventional off-axis electron holography, the phase shift of a plane electron wave due to transmission through an electrostatic potential (magnetic vector potential) is reconstructed from an interference pattern, the hologram, created in the image plane. Thereby, the sample of interest is placed off the optical axis in the microscope's electron column operated in TEM mode. Since the sample is placed only in one half-plane, usually only the respective part of the plane wave is altered by the presence of the sample. The part of the wave trespassing the other half-plane of the column ideally remains unaffected by the specimen and is often considered constant in phase and amplitude. Because this study deals with long-range electric fields, a strict separation of specimen and reference region is not assumed initially. Instead we propagate also an arbitrary reference wave through the description of hologram formation and study the impact of common approximations below. To form the hologram, the object wave and reference wave are tilted towards each other and brought to interference by a Möllenstedt–Düker biprism [18] which is set to positive voltage.

In the detector plane, the object wave can be expressed by $\Psi_\mathrm{obj} = A(\vec{r}_\perp) e^{i\vec{k}_{\perp,\mathrm{obj}} \cdot \vec{r}_\perp + i\Phi_\mathrm{obj}(\vec{r}_\perp)}$, and the reference wave by $\Psi_\mathrm{ref}(\vec{r}_\perp) = A_0(\vec{r}_\perp) e^{i\vec{k}_{\perp,\mathrm{ref}} \cdot \vec{r}_\perp + i\Phi_\mathrm{ref}(\vec{r}_\perp)}$. Here, $\vec{r}_\perp = (x, y)$ denotes a two-dimensional vector in the detector plane perpendicular to the optical axis and $\vec{k}_\perp$ the lateral component of the wave vector due to the tilt by the biprism. $A(\vec{r}_\perp)$ and $A_0(\vec{r}_\perp)$ signify the amplitudes of the wave functions Ψ_obj and Ψ_ref, respectively. $\Phi_\mathrm{obj}(\vec{r}_\perp)$ and $\Phi_\mathrm{ref}(\vec{r}_\perp)$ denote the phase distributions of the object wave and the reference wave, where the central quantity to be recovered is $\Phi_\mathrm{obj}(\vec{r}_\perp)$. From the emerging interference pattern (hologram), the relative phase shift between the waves at each position $\vec{r}_\perp$ in the detector plane can be inferred via

$$\begin{aligned} I_\mathrm{holo} &= |\Psi_\mathrm{obj} + \Psi_\mathrm{ref}|^2 \\ &= A_0^2(\vec{r}_\perp) + A^2(\vec{r}_\perp) \\ &\quad + A_0(\vec{r}_\perp) A(\vec{r}_\perp) \cdot \exp(i\Delta\Phi(\vec{r}_\perp)) \\ &\quad + A_0(\vec{r}_\perp) A(\vec{r}_\perp) \cdot \exp(-i\Delta\Phi(\vec{r}_\perp)) \, . \end{aligned} \tag{7}$$

We write the phase difference $\Delta\Phi(\vec{r})$ between both waves evaluated at $\vec{r}_\perp$ in the detector plane as

$$\begin{aligned} \Delta\Phi(\vec{r}_\perp) &= (\vec{k}_{\perp,\mathrm{obj}} - \vec{k}_{\perp,\mathrm{ref}}) \cdot \vec{r}_\perp \\ &\quad + \Phi_\mathrm{obj}(\vec{r}_\perp) - \Phi_\mathrm{ref}(\vec{r}_\perp) \\ &= \vec{k}_{\perp,\mathrm{C}} \cdot \vec{r}_\perp + \Delta\varphi(\vec{r}_\perp) \, . \end{aligned} \tag{8}$$

In $\Delta\varphi(\vec{r}_\perp)$, the object phase is encrypted, which is aimed to be reconstructed from the recorded hologram. The reconstruction follows in essential aspects the so called single side-band reconstruction (SSB) [11, 19]. Thereby, the hologram is Fourier-transformed resulting in one central band and two side bands in reciprocal space. One side band is masked by a (digital) circular aperture B and centred, which effectively removes the carrier frequency $\vec{k}_{\perp,C}$ from the phase difference $\Delta\Phi(\vec{r}_\perp)$. Via an inverse Fourier-transformation of the centred and masked side band, the reconstructed wave function is given by

$$\Psi_\mathrm{rec}(\vec{r}_\perp) = A_0(\vec{r}_\perp) A(\vec{r}_\perp) \cdot \exp(i\Delta\varphi(\vec{r}_\perp)) \otimes B(\vec{r}_\perp) \, . \tag{9}$$

Hence, the reconstructed wave function Ψ_rec contains the relative phases of the object wave and reference wave, their mutual amplitude distribution and a convolution with the reconstruction aperture assuming absence of aberrations here. This is justified due to the low spatial frequencies that build up the long-range fields under study. At in-focus conditions and assuming the interaction to be described by a phase object the amplitudes A and A_0 are constant and equal to 1, such that Eq. (9) reads

$$\Psi_\mathrm{rec}(\vec{r}_\perp) \approx \exp(i\Delta\varphi(\vec{r}_\perp)) \otimes B(\vec{r}_\perp) \, . \tag{10}$$

Note that the phase of Ψ_rec is formally in general not necessarily equal to $\Delta\varphi(\vec{r}_\perp)$ due to the convolution with the aperture. However, a more direct relation between the phase of Ψ_rec and $\Delta\varphi(\vec{r}_\perp)$ can be obtained in two ways. First, in case $\exp(i\Delta\varphi(\vec{r}_\perp))$ is band limited, one can choose $B(\vec{r}_\perp)$ large enough such that the convolution has no effect. In that case,

$$\Psi_\mathrm{rec}(\vec{r}_\perp) \approx \exp(i\Delta\varphi(\vec{r}_\perp)) \quad , \tag{11}$$

by similar arguments that lead to Eq. (6). Second, the weak phase object yields

$$\begin{aligned} \Psi_\mathrm{rec}(\vec{r}_\perp) &\approx (1 + i\Delta\varphi(\vec{r}_\perp)) \otimes B(\vec{r}_\perp) \\ &\approx 1 + i\Delta\varphi(\vec{r}_\perp) \quad , \end{aligned} \tag{12}$$

where the second line is valid for the band limited case. The present study deals with long-range fields, implying the neglect of $B(\vec{r}_\perp)$ here, such that Eqs. (9), (12) govern the interpretation of the reconstructed wave.

In fact, since $\Delta\varphi = \Phi_\mathrm{obj}(\vec{r}_\perp) - \Phi_\mathrm{ref}(\vec{r}_\perp)$, the reconstruction only delivers the pure phase of the object-side half-plane of the biprism if $\Phi_\mathrm{ref}(\vec{r}_\perp) = \mathrm{const.}$, i.e., a plane reference wave. Consequently,

$$\Psi_\mathrm{rec}(\vec{r}_\perp) \approx \exp(i\Phi_\mathrm{obj}(\vec{r}_\perp)) \approx 1 + i\Phi_\mathrm{obj}(\vec{r}_\perp) \tag{13}$$

holds only for band limited signals, phase or weak phase objects, respectively, and an unperturbed reference wave. Finally, this yields the projected potential via $\Phi_\mathrm{obj}(\vec{r}_\perp) = \sigma V_\mathrm{p}(\vec{r}_\perp)$ with the interaction constant σ.

To conclude these abstract methodological considerations of field measurements in FM STEM and EH partly involve different approximations and strategies to provide projected electric field and projected

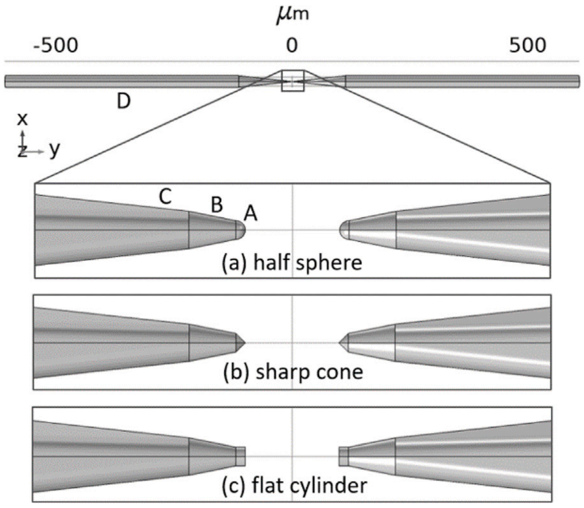

Fig. 2. Needle models used within the FE simulation. The opposing needles are identical and rotationally symmetric. The capital letters A, B, C and D indicate the compounded needle parts. The cases (a), (b) and (c) show needles with differently shaped tips. The needle length is chosen such that $E^{\mathrm{FE}}_{\mathrm{p,y}}$ converges between needles (614 μm).

potential relative to a reference. Whereas the accuracy of the STEM technique relies on a subsequently performed scan under field-free (or known) conditions, at least standard EH requires a field-free aloof region for the reference wave during the single acquisition. In cases where it is uncertain that the setup fulfils this condition for the reference wave, Eqs. (10), (13) must be considered. Here, the hologram recorded with biased needles has been corrected using a hologram with identical settings, however, with the needle voltage at 0 V. It has to be noted that the taken reference does not remove the PRE from the original hologram. The measured phase $\Delta\varphi$ needs to be interpreted by accompanying simulations then in which the large-scale potential distribution is modelled as detailed in the following two subsections on FE simulations and a summary of the analytical line charge approach.

2.4. *Finite element simulations*

The electrostatic potential V^{FE} and related quantities have been derived numerically via FE simulations corresponding to the biased needle setup introduced in Fig. 1a. Both needles have been assumed to be identical and rotationally symmetric, each modelled in four parts (A–D) as shown in Fig. 2. The tip is either modelled as half sphere, cone or cylinder (A) and continues with a short conical section (B) as tip extension. Another conical section (C) with smaller opening angle follows, adapted from the experimental needle shape, which finally merges into a cylindrical rod (D) of constant diameter which is chosen as 25 μm according to the manufacturers specification.

A simulated 3D section of the electric potential V^{FE} around the biased needles is shown in Fig. 3a. By projection of V^{FE} along the z-direction, the projected potential $V^{\mathrm{FE}}_{\mathrm{p}}$ of the whole simulation volume is obtained (Fig. 3b). Subsequently, the projected electric field $\vec{E}^{\mathrm{FE}}_{\mathrm{p}}$ is given by the gradient of $V^{\mathrm{FE}}_{\mathrm{p}}$ in x- and y-direction.

Fig. 3c shows a map of the obtained projected electric field $E^{\mathrm{FE}}_{\mathrm{p,y}}$ pointing in y-direction. Throughout this study, $E^{\mathrm{FE}}_{\mathrm{p,y}}$ is evaluated along the dashed line profile at the half axis which hereafter itself is denoted as $E^{\mathrm{FE}}_{\mathrm{p,y}}$ being one-dimensional. In the further course, respective simulation parameters are given where appropriate in the corresponding sections.

2.5. *Analytic line charge model*

Complementary to the FE simulation, an analytic line charge model (LCM) [16] has been employed as a possible alternative to the customised FE simulation above. This was done to revise whether a computationally much less demanding procedure could be used to interpret experiments quantitatively. In the framework of the LCM, a biased needle of the setup in Fig. 1 is approximated as an infinitesimally thin line with length d and constant line charge density δ_{LCM}. The electrostatic potential V^{LCM} can be expressed analytically as

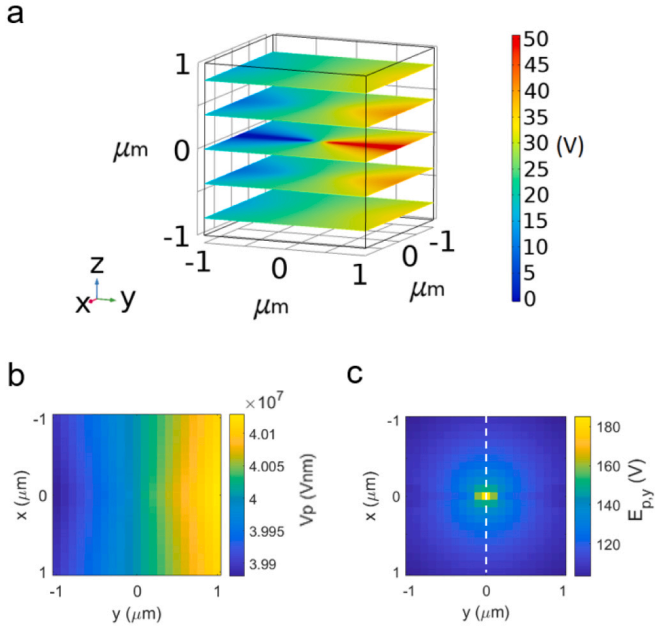

Fig. 3. (**a**) Selected 3D section of the electrostatic potential V^{FE} numerically derived by FE simulation. (**b**) Projected electrostatic potential $V^{\mathrm{FE}}_{\mathrm{p}}$ yielded by projection of V^{FE} along z-direction. (**c**) Projected electric field $E^{\mathrm{FE}}_{\mathrm{p}}$ in y-direction via gradient of $V^{\mathrm{FE}}_{\mathrm{p}}$. $E^{\mathrm{FE}}_{\mathrm{p,y}}$ is evaluated along the dashed line profile.

$$V^{\mathrm{LCM}} = \frac{\delta_{\mathrm{LCM}}}{4\pi\epsilon_0} \cdot \log\left[\frac{\sqrt{x^2+(d+y)^2+z^2}+d+y}{\sqrt{x^2+y^2+z^2}+y}\right]. \tag{14}$$

For the comparative application of the LCM, the line charge density has to be specified which favourably is chosen according to the present needle setup. Here, the line charge density δ_{LCM} is experimentally derived via EH according to Ref. [20], being insensitive to the PRE, as long as the region from which the reference wave is obtained is itself charge-free. This yields an effective line charge density δ_{EH}, which amounts to 3.26 e/nm for the introduced setup.

Fig. 4 shows contour plots of V^{LCM} in the x–y-plane at position $z = 0$, generated by two line charges with opposite charging $\pm\delta_{\mathrm{EH}}$. These fictitious needles are indicated as equipotential surfaces of −25 V (left) and 25 V (right) to emulate the potential difference of 50 V present between the needles in experiment. The corresponding analytical expression for the projected electrostatic potential $V^{\mathrm{LCM}}_{\mathrm{p}}$ is given by

$$\begin{aligned} V^{\mathrm{LCM}}_{\mathrm{p}} = \frac{\delta_{\mathrm{LCM}}}{4\pi\epsilon_0} \cdot \Big[&-(d+y)\log\left(x^2+(d+y)^2\right) \\ &+ y\log\left(x^2+y^2\right) + 2d + 2x\tan^{-1}\left(\frac{y}{x}\right) \\ &- 2x\tan^{-1}\left(\frac{d+y}{x}\right)\Big]. \end{aligned} \tag{15}$$

In Section 3.4, the validity of the LCM applied to the presented needle setup is discussed by means of a comparison to the FE results.

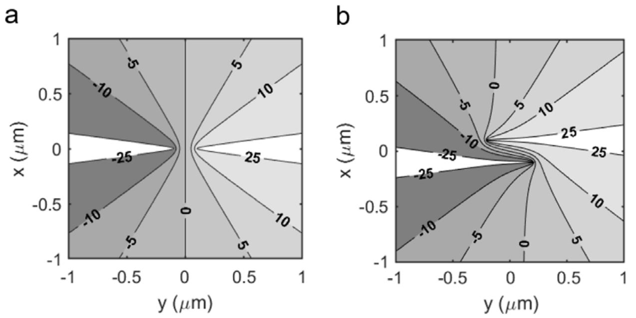

Fig. 4. Contour plots of V^{LCM} generated by two oppositely charged line charges in the x–y-plane at position $z = 0$. The contours represent the cross-section of the x–y-plane and equipotential surfaces of V^{LCM} tagged with the respective value in Volt. (**a**) Line charges mirrored at x-axis with 200 nm gap at position x=0. (**b**) Line charges parallelly aligned to y-axis with tips at $y = \pm 200$ nm and lateral positioned at $x = \mp 100$ nm.

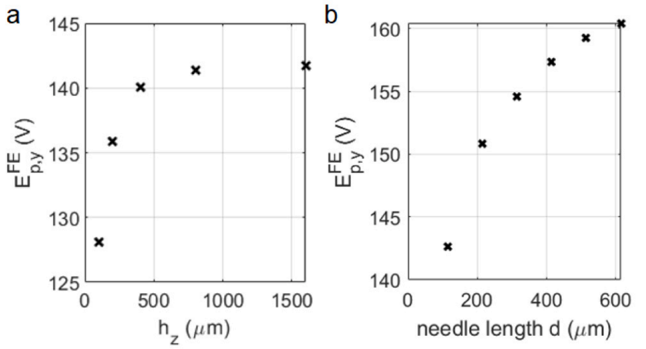

Fig. 5. Convergence study to the projected electric field $E^{\mathrm{FE}}_{\mathrm{p,y}}$ derived via FE simulation regarding the projection volume height h_z and the needle length d. Peak value of $E^{\mathrm{FE}}_{\mathrm{p,y}}$ between needles plotted in (**a**) for increasing height h_z of the projection volume symmetrically around $z = 0$ and subsequently in (**b**) for simultaneously increasing the length d of both needles at $h_z = 1.6$ mm.

3. Results

3.1. Convergence of the electric field in FE simulations

Essentially, a numerically converged solution of the projected electrostatic potential is to be obtained. Initially, the 3D potential V^{FE} is derived via FE simulation solely relying on geometric and electrostatic boundary conditions as input parameters. To calculate the projected electrostatic potential $V^{\mathrm{FE}}_{\mathrm{p}}$ and subsequently the projected electric field $\vec{E}^{\mathrm{FE}}_{\mathrm{p}}$, a projection volume of finite height h_z in z-direction needs to be defined within the simulation, such that a sufficiently large fraction of the electric field is collected in $\vec{E}^{\mathrm{FE}}_{\mathrm{p}}$ via projection as the electric field has infinite spatial reach and asymptotically decreases with $\frac{1}{h_z^2}$.

On the one hand, the height of the projection volume in z-direction has to be large enough for the projected electric field to reach convergence. On the other hand, the needle length d needs to be increased until convergence is reached. This is because more distant parts of the needles also contribute to the electric field between the needles. Note that the needles used in the experiment are of macroscopic lengths.

In Fig. 5a, the peak value of the projected electric field $E^{\mathrm{FE}}_{\mathrm{p,y}}$ at the centre between both needles is plotted against h_z. The projection volume height h_z was increased stepwise, symmetrically around the position $z = 0$ with needles of 114 μm length. At $h_z = 1.6$ mm, $E^{\mathrm{FE}}_{\mathrm{p,y}}$ is sufficiently converged. It is noteworthy that about 90% of $E^{\mathrm{FE}}_{\mathrm{p,y}}$ is contained within a projection volume of 100 μm height whereas the remaining 10% are spread over the macroscopic distance of 1.6 mm. In Fig. 5b, the rod part of the needle (Fig. 2D) has been increased in length. At a total needle length of 614 μm, $E^{\mathrm{FE}}_{\mathrm{p,y}}$ is sufficiently converged. Here, the major abort condition regarding the convergence is the balance between accuracy and increasing numerical effort due to larger needles and projection volume resulting in slight underestimation of $E^{\mathrm{FE}}_{\mathrm{p,y}}$. In conclusion, the field spreads over a millimeter-sized region which implies a challenge for the investigation of nanostructures, since interaction distances scale over six orders of magnitudes.

3.2. Impact of needle geometry on projected electric field

In the following, changes in projected electric field $E^{\mathrm{FE}}_{\mathrm{p,y}}$ introduced by variations to the needle geometry and their relative position are studied using FE simulations. Fig. 6a shows the evolution of $E^{\mathrm{FE}}_{\mathrm{p,y}}$ when the gap distance between the needles is varied along the y-axis. With decreasing gap distance, $E^{\mathrm{FE}}_{\mathrm{p,y}}$ increases drastically at the origin of the x-axis. Approximately 200 nm apart from the origin in x-direction, the line profiles of $E^{\mathrm{FE}}_{\mathrm{p,y}}$ approach the same value for different gap distances. During an experiment, it cannot be assumed that the tips are perfectly aligned vertically and laterally as being symmetrically mirrored at the x–z-plane. Therefore, the influence of relative misalignment of the needles on $E^{\mathrm{FE}}_{\mathrm{p,y}}$ is studied as well. Thereby, one needle (left) remains at its original position while the other one (right) is shifted along the x- and z-direction. Fig. 6b shows that a relative needle shift in x-direction reduces and shifts the maximum of $E^{\mathrm{FE}}_{\mathrm{p,y}}$ significantly which lays at half the position of the total shift distance. Furthermore, shifting the needle by up to 150 nm in x-direction leads to a considerable broadening of the peak. Beyond a relative shift of 150 nm, the peak starts to separate into two peaks of equal height.

In Fig. 6c, exclusively shifting the needle in z-direction shows that $E^{\mathrm{FE}}_{\mathrm{p,y}}$ is far more sensitive to relative needle shifts in x-direction as compared to shifts along z. Even a shift of 1 μm in z-direction leads to a reduction of about 8 V in $E^{\mathrm{FE}}_{\mathrm{p,y}}$ comparing peak values, being only 5% of the unshifted case. In x-direction, a shift of about 150 nm is sufficient to likewise reduce $E^{\mathrm{FE}}_{\mathrm{p,y}}$.

Additionally, the influence of the tip shape on $E^{\mathrm{FE}}_{\mathrm{p,y}}$ has been evaluated by simulating two more tip geometries, apart from the original half sphere which have been presented in Fig. 2. The result of the half sphere, a flat cylinder and a sharp cone are plotted in Fig. 6d. The evolution of the peak values of $E^{\mathrm{FE}}_{\mathrm{p,y}}$ shows that the specific tip shape becomes less important with increasing gap distance. For smaller needle separations, sharpening the tip from cylindrical shape over a hemisphere to a cone generates a considerably lower projected electric field. For the tip distance of approximately 200 nm used in the experiment as depicted in Fig. 1a, the slightly, yet overtly, different tip shapes should therefore have minor impact on the measured projected electric field.

3.3. Potential quantification by EH and PRE

With the above FE results for long-range electric field geometries and needle architectures in mind, we now address the measured fields in Fig. 1b quantitatively of which here the EH measurement is focused on. Fig. 7a shows a 2D map of the projected electric potential $V^{\mathrm{FE}}_{\mathrm{p}}$ yielded by an FE simulation for a tip distance of 200 nm and a bias of 50 V. In the context of EH, the regions **O** and **R** indicate the areas of the object wave and the reference wave according to the experiment, which are brought to interference in the image plane. Both areas are of same size and of the same width w corresponding to the width of the resulting interference region. Here, a fictitious biprism is assumed to be located at $x = w/2$ parallel to the y-axis. Since the reference wave is rather represented by a part of the FE simulation than assumed to have a flat phase, the perturbed reference wave effect is included in the present analysis.

Eq. (8) represents the general phase difference between object wave and reference wave encrypted in the hologram. Neglecting the carrier-frequency after reconstruction yields

$$\Delta\varphi(\vec{r}_\perp) = \Phi_{\mathrm{obj}}(\vec{r}_\perp) - \Phi_{\mathrm{ref}}(\vec{r}_\perp)\,. \tag{16}$$

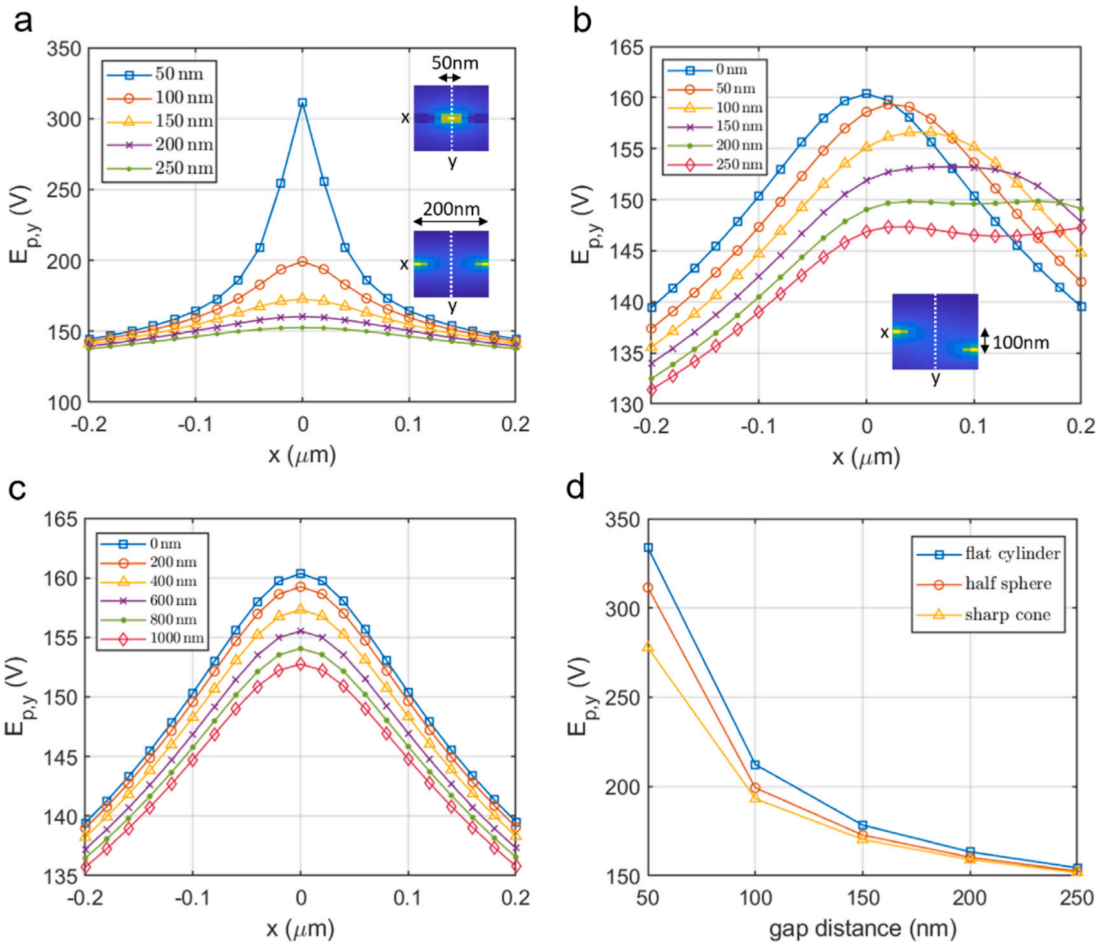

Fig. 6. The projected electric field $E^{\mathrm{FE}}_{\mathrm{p,y}}$ is shown (**a**) for different gap distances between the needles (50–250 nm) without a relative needle shift in x- and z-direction, (**b**) for different needle shifts in x-direction (50–250 nm) at constant gap distance of 200 nm without shift in y- and z-direction, (**c**) for different needle shifts in z-direction between the needles (0-1 µm) at 200 nm gap distance without needle shift in x- and y-direction, and (**d**) shows the dependence of $E^{\mathrm{FE}}_{\mathrm{p,y}}$ from the used tip shape. Analogous to (**a**), the maximal value of $E^{\mathrm{FE}}_{\mathrm{p,y}}$ between the needles is plotted against the gap distance without needle shift in x- and z-direction. This is depicted for each of the three different tip shapes.

Assuming a phase object, the phase shifts owing to the projected electrostatic potential V_{p} trespassed by the object wave and reference wave read

$$\Phi_{\mathrm{obj}}(\vec{r}_\perp) = \sigma V_{\mathrm{p}}(\vec{r}_\perp) \tag{17}$$

$$\Phi_{\mathrm{ref}}(\vec{r}_\perp) = \sigma V_{\mathrm{p}}(\vec{r}_\perp + w \cdot \vec{e}_x)\,. \tag{18}$$

In this simulation study, we neglect the finite wire diameter of the biprism amounting to 160 nm backprojected to the object plane, being much smaller than the experimental overlap width w of several microns. The encrypted projected electrostatic potential in the hologram is accordingly given by

$$V_{\mathrm{p}}^{\mathrm{EH,PRE}}(\vec{r}_\perp) = \Delta\varphi/\sigma = V_{\mathrm{p}}(\vec{r}_\perp) - V_{\mathrm{p}}(\vec{r}_\perp + w \cdot \vec{e}_x)\,. \tag{19}$$

Inserting $V_{\mathrm{p}}^{\mathrm{FE}}$ on the right hand side yields the counterpart simulated by FE. Fig. 7b exemplarily shows the expected projected potential $V_{\mathrm{p}}^{\mathrm{FE,PRE}}$ after region **O** and **R** have been brought to interference for a widths w of the interference region. Eventually, Fig. 8 shows the line plots between the needles of the unperturbed electric field $E^{\mathrm{FE}}_{\mathrm{p,y}}$ after taking the gradient of the potential, the perturbed field $E^{\mathrm{FE,PRE}}_{\mathrm{p,y}}$ and the experimental $E^{\mathrm{EH}}_{\mathrm{p,y}}$ measurement. Here, w is chosen to 2.4 µm in correspondence to the experiment. The EH measurement of $E^{\mathrm{EH}}_{\mathrm{p,y}}$ is well reproduced by $E^{\mathrm{FE,PRE}}_{\mathrm{p,y}}$ from FE simulation when the PRE is considered. Furthermore, the unperturbed $E^{\mathrm{FE}}_{\mathrm{p,y}}$ is as well in good agreement with the COM measurement $E^{\mathrm{COM}}_{\mathrm{p,y}}$ shown in Fig. 9.

3.4. Validity of analytical line charge model

The computational effort of the FE studies suggests testing to which extent the LCM is capable of a quantitative reproduction of the PRE and the experimental observations. According to Eq. (14), the model contains only three parameters which are the needle length d, the line charge δ_{LCM} and the relative needle shift when superimposing multiple needle potentials. Here, two needle lengths have been chosen to 100 µm and 614 µm. The former is commonly assumed to yield suitable results in practice, whereas the latter provided the best agreement with the present experiment and, interestingly, corresponds to the FE simulation. In Fig. 10, the respective projected electric fields $E^{\mathrm{COM}}_{\mathrm{p,y}}$ from COM measurement, $E^{\mathrm{FE}}_{\mathrm{p,y}}$ from FE simulation and $E^{\mathrm{LCM}}_{\mathrm{p,y}}$ from LCM are juxtaposed. However, with a needle length of 614 µm, the maximum and the reduction of the measured field in its vicinity is represented rather well by the LCM, but nevertheless differs significantly beyond 100 nm aloof the symmetry point $x = 0$.

Moreover, in analogy to δ_{LCM}, an effective line charge density δ_{FE} can be obtained from the conducted FE simulation. Fig. 11 shows the surface charge from FE evaluated within the x–y-plane at $z = 0$. Azimutal integration of the surface charge along the needle in y-direction results in the effective line charge density δ_{FE} which amounts to 2.15 e/nm which is approximately two thirds of the corresponding experimental result of 3.26 e/nm measured via EH.

Even though qualitatively good results can be obtained, the LCM here is not able to reproduce the details of the profile quantitatively.

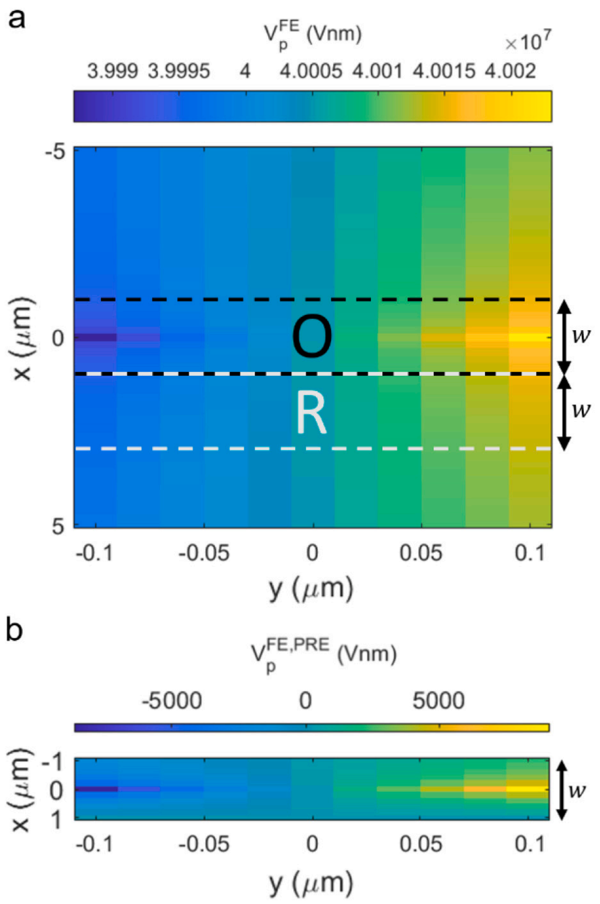

Fig. 7. (**a**) 2D map of the projected electric potential V_p^{FE} between the biased needles. Region **O** and **R** represent the areas which are propagated by an object wave and a reference wave, respectively, within EH. (**b**) 2D map of the perturbed projected electric potential $V_p^{FE,PRE}$ obtained by superposition of V_p^{FE} in region **O** and **R** with interference region width w.

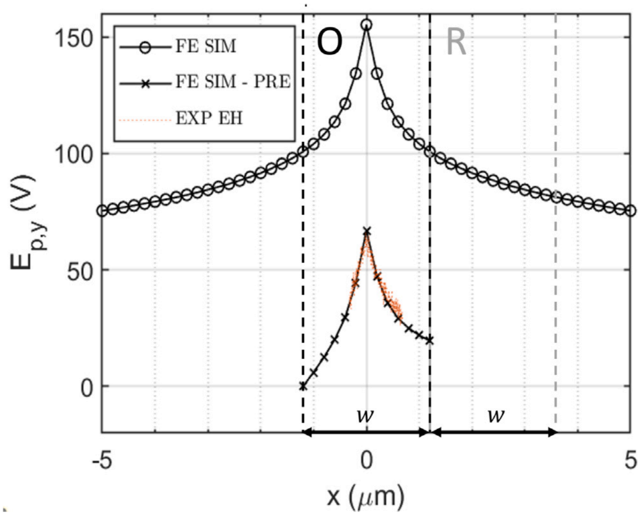

Fig. 8. Projected electric field $E_{p,y}^{EH}$ plotted from FE simulation (FE SIM), the FE simulation altered by the perturbed reference wave effect (FE SIM-PRE) and experimentally measured by off-axis EH (EXP EH). **O** and **R** indicate the lateral regions which are propagated by the object wave and reference wave in EH, respectively, w indicates the width of the interference region.

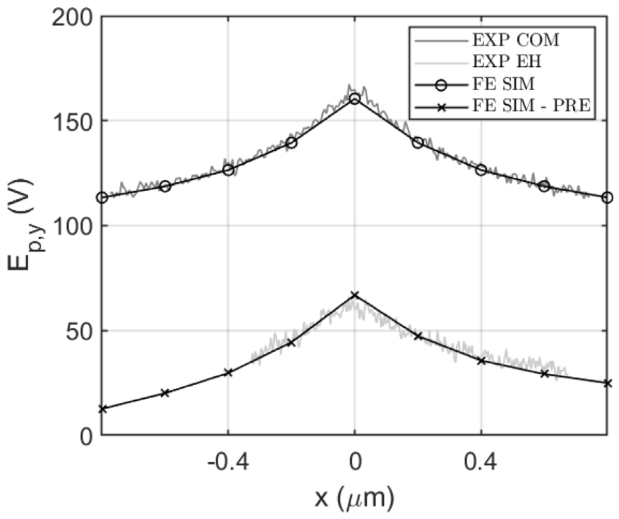

Fig. 9. Collection of the projected electric fields $E_{p,y}$ from the experimental COM measurement (EXP COM), the experimental EH measurement (EXP EH), FE simulation (FE SIM) and the perturbed FE simulation (FE SIM-PRE).

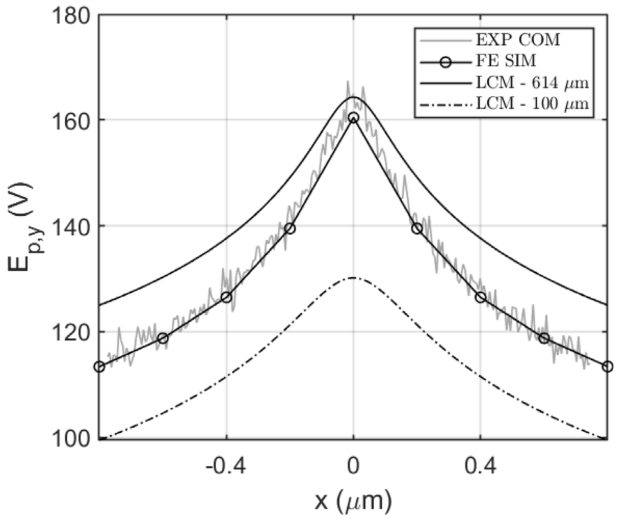

Fig. 10. Projected electric field $E_{p,y}$ plotted from the experimental COM measurement (EXP COM), FE simulation (FE SIM), the line charge model with different needle lengths (LCM - 100 μm, LCM - 614 μm).

Reasons for the inaccuracies of the LCM are the insufficiently specified needle length and the principle lack of geometrical boundary conditions, leading to a mismatch of the shapes of the equipotential surface at a given bias voltage and the needle surface.

3.5. COM simulation

As seen in Fig. 9, the experimental COM signal agrees well with the unperturbed FE simulation result $E_{p,y}^{FE}$. However, the COM signal may depend on the chosen microscope parameters which may impact the STEM-probe's sensitivity to the probed electric field as its spatial profile is altered, just as the EH signal is subject to the reconstruction aperture, or a physically inserted objective aperture. Multislice simulations [21] are employed in the following to analyse the impact of the acceleration voltage in the range of 100 to 300 kV, semi-convergence angle and the phase object approximation on the COM signal. The simulations were carried out in a volume with dimensions of 800 nm × 800 nm × 100 μm, sampled with 10000 × 10000 × 500 pixels. The sampling within the x–y-plane has been heightened by numerical interpolation

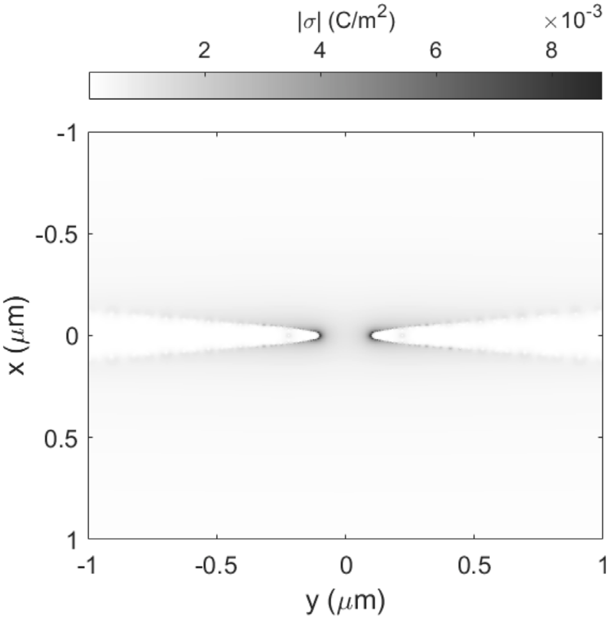

Fig. 11. Magnitude of the surface charge σ at both needle surfaces yielded via FE simulation. In particular, a cross-section of the needle setup is shown in the x–y-plane at height $z = 0$.

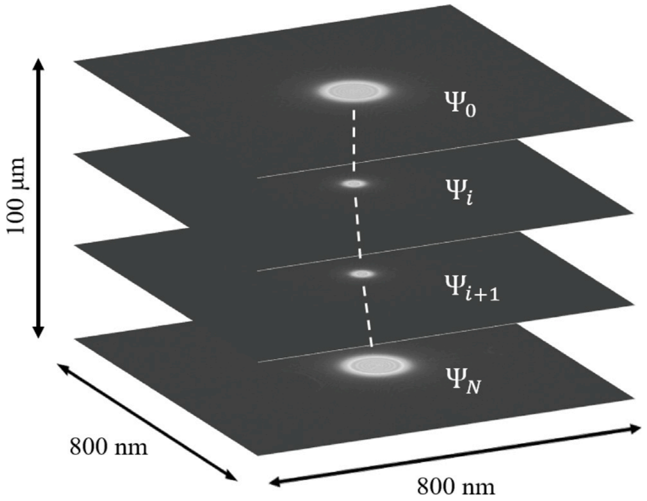

Fig. 12. Illustration of the multislice simulation for an incident STEM-probe Ψ_0 at 100 kV acceleration voltage and 1 mrad semi-convergence angle propagated iteratively through 3 slices. The simulation takes place within a volume of dimensions 800 nm × 800 nm × 100 μm sampled by 10000 × 10000 × 500 pixels. Ψ_0 is focused at the centre of the volume (−50 μm).

which is feasible as the potential landscape is slowly varying. Within the multislice scheme, the simulation volume is vertically separated into slices containing the corresponding electric potential, here V^{FE} from the FE simulation. For each slice i, the projected electrostatic potential $V^{\mathrm{FE}}_{\mathrm{p,i}}$ is calculated which acts as phase object within the MS. Via the Fresnel-propagator, the phase-shifted probe is propagated to the adjacent slice $i+1$ until the whole volume has been transmitted.

Fig. 12 illustrates the MS scheme for the intensities of the incident STEM probe Ψ_0 and succeeding exit waves after each slice in the corresponding x–y-planes for 100 kV acceleration voltage and 1 mrad semi-convergence angle. Besides, the incident STEM probe was focused to the centre of the simulation volume. Hence, the MS starts with a defocused STEM probe at $z = -50$ μm at the top of the interaction volume, therefore, having an increased probe diameter vertically off the centre. Here, at each slice the lateral probe shift s_{lat} induced by the transmitted electric field to the probe is determined. As elaborated in Section 2, the Fourier transform of an exit wave Ψ_{ex} in STEM corresponds to the diffraction pattern in the detector plane from which here the COM signal $\vec{E}^{\mathrm{MS,COM}}_{\mathrm{p,i}}$ is calculated.

In Fig. 13, the projected electric potential $E^{\mathrm{FE}}_{\mathrm{p,y}}$ accumulated along the z-direction from the FE simulation is shown, together with the COM signal $E^{\mathrm{MS,COM}}_{\mathrm{p,y}}$ and the lateral beam shift s_{lat} calculated via MS for each slice. In particular, $E^{\mathrm{FE}}_{\mathrm{p,y}}$ is exemplarily plotted for 5 and 500 slices in Fig. 13a. The respective electrostatic potential V^{FE} is used to calculate the respective slice-wise phase grating by projection along z for the MS simulation. The calculated COM signal for different numbers of slices is depicted in Fig. 13b. Obviously, the number of slices has negligible impact on the COM signal, since all curves yield the same projected electric field value of $E^{\mathrm{MS,COM}}_{\mathrm{p,y}}$ (127 V) after passing the whole interaction volume at $z = 50$ μm. Furthermore, Fig. 13c shows the lateral probe shift at each slice as determined by the COM in real space. Here, five slices were used and the MS simulation was done for semi-convergence angles ranging from 1–4 mrad. As the strongest contribution of the electric field lays between $z = \pm 10$ μm, the probe gets perceptibly shifted in that region, whereas for $z < -10$ μm only minor shifts can be observed. For $z > +10$ μm, the probe has already acquired a lateral momentum by which the probe is further shifted laterally during the ongoing propagation, while simultaneously acquiring marginal additional momentum by the decreasing stray electric field. Interestingly, Fig. 13c reveals that higher semi-convergence angles here result in larger beam shifts at constant acceleration voltage and slicings.

Additional trends in the simulated COM signals and lateral probe shifts are examined in more detail in Fig. 14.

For 100, 200 and 300 keV electron energy and using the single-slice projection assumption which is justified according to Fig. 13, $E^{\mathrm{MS,COM}}_{\mathrm{p,y}}$ and the lateral translation of the probe s_{lat} are shown in Fig. 14a and b, respectively. Whereas $E^{\mathrm{MS,COM}}_{\mathrm{p,y}}$ varies only at the second digit, it increases slightly with increasing semi-convergence angles between 1–5 mrad. The probe shift s_{lat} gets larger with increasing semi-convergence angle and decreasing acceleration voltage as well. In the ensuing discussion, these findings are further elaborated.

4. Discussion

Impact of needle geometry on projected electric field

Section 3.2 showed that reducing the gap distances between the needles increases the projected electric field $E^{\mathrm{FE}}_{\mathrm{p,y}}$ locally at the origin, whereas $E^{\mathrm{FE}}_{\mathrm{p,y}}$ evaluated off centre remains mainly unaffected. For small gap distances, it was demonstrated that the mere tip shape can have a strong impact on $E^{\mathrm{FE}}_{\mathrm{p,y}}$. Regarding the reproducibility of an experiment, it is thus advisable to choose a gap distance at which the projected electric field between the needles is not sensitive to the details of the needle's tip shape. Note that an experimenter has limited control over the geometry of the biasing architecture at the nanometre scale, e.g., using etching methods or mechanical procedures.

Furthermore, probing stray electric fields via STEM is commonly carried out at low semi-convergence angles which compels a large focus depth of the STEM-probe reaching microns. Experimentally, this hampers the alignment of the biasing setup in z-direction. Fortunately, it was shown that $E^{\mathrm{FE}}_{\mathrm{p,y}}$ is far less sensitive to relative needle shifts in z-direction compared to shifts in x-direction, here the difference was a factor of approximately seven.

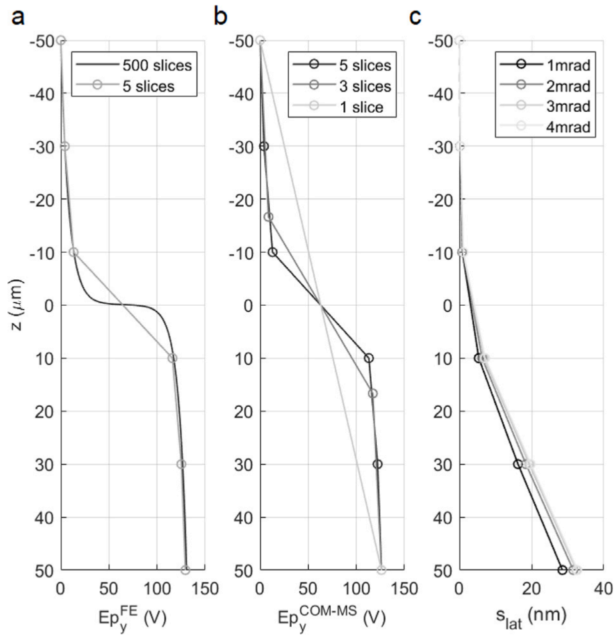

Fig. 13. (**a**) Projected electric field $E_{p,y}^{FE}$ accumulated in z-direction from top to bottom of the simulated propagation volume used as input for MS showed for 5 and 500 slices. (**b**) COM signal $E_{p,y}^{MS,COM}$ from multislice simulation evaluated for 1, 3 and 5 slices with STEM-probe of 1 mrad at 100 kV. (**c**) Lateral beam shift s_{lat} from multislice simulation due to deflection by the electric field shown for 1–4 mrad STEM-probes.

In principle, a variation study of the setup geometry is conductible experimentally, too. Nonetheless, asymmetric tips and uncertainties to estimate the relative needle position hardens the interpretation of results and their applicability to alike setups. A remedy would be the acquisition and the subsequent 3D shape reconstruction of a tomographic tilt series.

Potential quantification by EH and PRE

It was found that the simulated unperturbed field $E_{p,y}^{FE}$ is in quantitative agreement with the COM measurement whereas the perturbed field $E_{p,y}^{FE,PRE}$ reduced by the PRE is in quantitative agreement with the EH measurement seen in Fig. 9. The obtained quantitative agreement of FE simulations with the experiments validates that the observed discrepancy between COM and EH here arises from the PRE.

In the past, Matteucci and coworkers [22] have proposed the use of analytic model simulations of electric potentials to reproduce the PRE seen in holography experiments. For simple experimental setups, analytical solutions to the electric potentials have been derived such that the PRE, observed in corresponding experiments, could be reproduced. Hence, electric field mapping via EH can be quantitatively interpreted when the PRE is posterior estimated.

In the present study, the projected potential between the biased needles can be regarded as a slowly varying strong phase as the total phase shift is $\sigma V_p^{FE} \approx 10^{-2} \cdot 4 \times 10^7 \gg 0.36$ which is given as 5% error limit applying the wPOA according to Ref. [23]. The phase shift of the perturbed potential can be estimated to $\sigma V_p^{FE,PRE} \approx 10^{-2} \cdot 8 \times 10^3 > 0.36$. Interestingly, the reduction of the total phase shift by the PRE favours the application of the wPOA. It is even possible to construct cases in which the wPOA is fully applicable altering the interference width w. Hence, on the one hand, the wPOA is mathematically strictly not justified here. On the other hand, the consistency between the COM measurement and the EH measurement when considering the PRE by means of FE simulations suggests a minor error of the reconstructed phase from experiment.

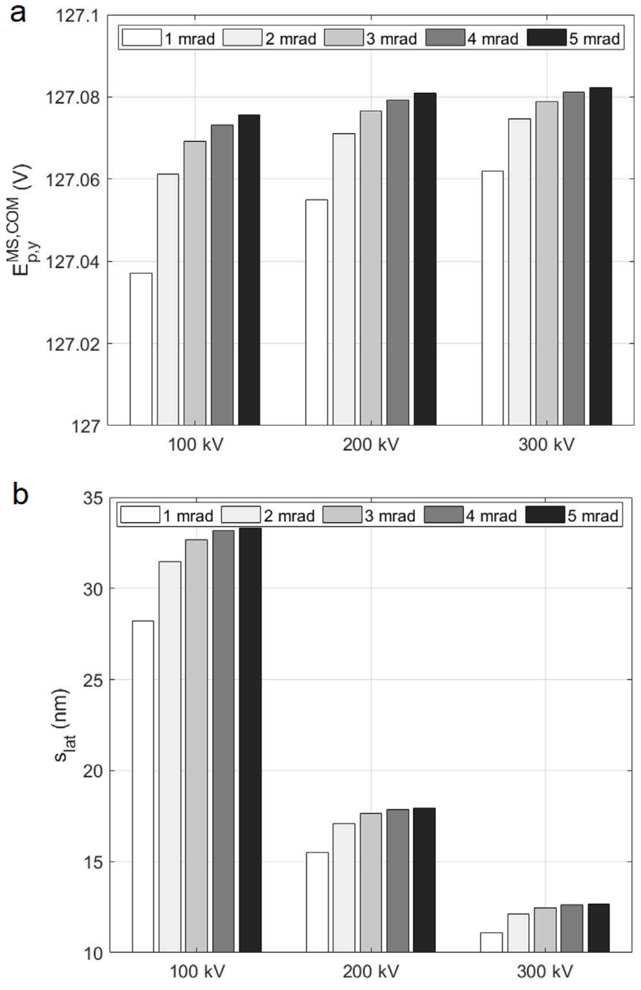

Fig. 14. (**a**) Projected electric field $E_{p,y}^{MS,COM}$ and (**b**) probe shift s_{lat} calculated via MS for an acceleration voltage of 100 kV, 200 kV and 300 kV. The incident probe Ψ_0 with semi-convergence angles between 1–5 mrad has been propagated through one slice of 100 μm height containing the needles in its centre.

Independently, another arising question is which approaches ought to be employed to reduce or eliminate the PRE posterior as well as anterior to an EH measurement. In Fig. 8, the line profiles have shown that the PRE reduces the estimated projected electric field drastically by about 57% comparing the peak values. Apparently, the percentage by which the projected electric field is reduced due to the PRE depends on the spatial profile of the unperturbed electric field and on the width w of the interference region. Therefore, a rather uneventful approach to reduce the PRE is to increase the lateral distance between the sample of interest and the reference wave. In conventional EH, this approach is limited by the partial coherence of the electron wave since object wave and reference wave have to be phase related in order to create a defined hologram via interference [24]. More advanced instrumentation and techniques in off-axis EH can be used to overcome related issues. To be mentioned is the technique known as split-illumination electron holography which uses multiple biprisms to acquire a coherent reference wave tens of microns away from the sample edge [25]. For microscopes still equipped with an conventional EH setup, an effectively more distant reference wave can be derived by an accumulated reconstruction method proposed by Harada and Kasai [26] in which multiple holograms are successively recorded ether shifting the sample or the biprism equidistantly, also enabling large FOV reconstructions.

Focusing again on the present EH setup, it has to be noted that once w is fixed, the percentage by which the PRE reduces the projected electric field cannot be changed by variation of the biasing voltage between the needles, leading to proportional scaling in magnitude only. However, to experimentally reduce the PRE, the gap distance between the needles can be reduced. This drastically increases the projected electric field close to the origin while the aloof field remains mainly unaffected, as seen in Section 3.2 for the present setup. On the contrary, decreasing the gap distance increases the dependence of the projected electric field between the needles on the tip geometry which has to be considered as well.

Under certain conditions, it is even possible to eliminate the PRE, without model-based simulations of long-range electric fields perturbing the reference wave, using the experimentally recorded hologram itself. Since Laplace's equation holds in vacuum, any potential landscape ideally needs to be describable by a superposition of harmonic functions. Employing a least squares approach, elimination of the PRE could be demonstrated by Kou and Chen [27]. Nevertheless, the practicability of the method is limited because the underlying electric potential has to be describable by such a mathematical basis set of functions and that very basis set has to be guessed. Furthermore, the electric potential has to be a continuous function, too, which excludes representing any transitions from sample to vacuum potential. In contrast, within a customised FE simulation, the potential is compulsory determined by geometrical boundary conditions which at least continuum-wise allow for transitions from vacuum to matter.

Validity of analytical line charge model

In Section 3.4, it was shown that the LCM is capable to yield qualitatively good results applied to the used needle setup. However, these model parameters do not represent the experimental ones accurately but had been determined such that consistency with the measured field profile can be achieved. Apart from choosing an appropriate line charge density and needle length in the LCM to achieve more accurate results, a key argument for the quantitative mismatch of the LCM with the COM measurement and the FE simulation is the principle incapability to set geometric boundary conditions to the charge distribution, for the charge in the LCM is always confined to an infinitesimally thin line. In that respect, the equipotential surfaces of the needles generated via LCM (Fig. 4) should correspond to the cross-section of the needles in the x–y-plane. Apparently, the equipotential surface does neither agree with the experiment (Fig. 1a) nor with the approximated geometry of the FE simulation (Fig. 11). Additionally, the equipotential surface within the LCM even changes its shape when the needles are shifted (Fig. 4b).

The above shortcomings of the LCM were also recognised by Tavabi et al. and others [16,28]. To achieve consistency between an aspired needle's shape used in experiment and the equipotential surface generate by a line charge potential, they adjusted the LCM parameters disregarding their associated physical correspondence. Subsequently, the obtained equipotential surface was artificially set to an appropriate value. This approach may be applicable as caustic effects have been regarded in their work taking place at the needles surface. However, scaling an appropriately shaped equipotential surface to the experimentally consistent value does not eventually yield a long-ranging potential landscape in free space which is also consistent with experiment.

Defying, F. Zheng et al. demonstrated that an iterative algorithm based on a line charge model is able to construct a charge distribution from an experimental electric charge measurement via EH also outside the field of view, e.g. of a metallic needle tip [29]. Subsequently, the electric field can be inferred by the constructed charge distribution without influence of the PRE. Thus, more advanced applications of the LCM might be able to accurately establish consistency with empirical data.

Nonetheless, the analytical LCM, regarded solely, yields qualitative results which can be generated with low computational effort and is especially beneficial in studies which demand smooth profiles over comparably large areas.

COM simulation

The MS showed that the electric field quantification via COM is stable under variation of the acceleration voltage, semi-convergence angle and the number of slices. The simulated projected electric field does not depend on the number of slices such that it is sufficient to apply the POA.

The lateral beam translation in real space decreases notably with increased acceleration voltage whereas the COM signal marginally increases in the sub-percent region for increasing acceleration voltage. Even though the magnitude of the COM signal is negligibly affected by the acceleration voltage, experimentally operating at lower acceleration voltages facilitates the COM measurement as larger beam shifts are easier detected [30]. Moreover, a minor dependency of the COM signal to the semi-convergence angle was noticeable. Increasing the semi-convergence angle from 1–5 mrad slightly increases the beam translation and the COM signal.

5. Conclusion

This study showed that numerical simulations based on a customised geometry, such as above conducted FE simulations, are a reliable tool to generate sufficiently accurate representations of stray electric fields corresponding to an experimental setup. For an experimentally measured projected electric field by conventional EH, it was demonstrated that the PRE needs to be taken into account accurately by FE simulations. In that way, consistency of projected electric field measurements via COM in STEM and EH, respectively, can be achieved. Contrary to an EH measurement, the electric field measurement via STEM does not suffer from PRE and yielded results which are consistent with the employed FE simulation of the electric field without additional modifications. Yet, PRE-related artefacts within the used EH setup can be overcome by more advanced EH techniques and instrumentation which lay outside the targeted principle comparison of stray electric field quantification between COM and conventional off-axis EH.

The use of the finite-element analysis via COMSOL enabled the simulation of long-range electric fields approaching macroscopic distances in the millimeter range. Other tools and differential equation solvers such as Liebmann solvers have been initially used [31] as the spatial evolution of the electric field in vacuum is fully determined by Laplace's equation for given electrostatic boundary conditions. Nevertheless, the simulative handling of electric fields across macroscopic distances with nano-metre resolution applying Laplace's equation numerically in real-space is computationally costly, for which the flexibly generated grid in FE is advantageous.

Disregarding the used field mapping method, COM or EH, custom model simulations are indispensable to quantify electric fields within biasing setups via TEM. On the one hand, stray electric fields might be artefact-inducing to a quantitative imaging method as seen in EH via the PRE. On the other hand, the stray electric fields generated by biasing architectures are generally superimposed with any other electric fields to be measured due to the projection of the measured signal in z-direction. As new correlative techniques emerge, for instance atom probe tomography conducted *in-situ* within the TEM, measurements involving biasing architectures crucially depend on the estimation of generated stray electric fields. The accurate understanding of both STEM and EH field mapping methods as presented in this work is thus not only a prerequisite to investigate stray fields in the established specimen geometries, but might also be relevant for future correlative microscopy techniques.

Declaration of competing interest

The authors declare the following financial interests/personal relationships which may be considered as potential competing interests: Knut Mueller–Caspary reports financial support was provided by Helmholtz Association of German Research Centres. Knut Mueller–Caspary reports financial support was provided by German Research Foundation. Jean Felix Dushimineza reports financial support was provided by Helmholtz Association of German Research Centres. Janghyun Jo reports financial support was provided by German Research Foundation.

Data availability

Data will be made available on request.

Acknowledgements

K. M.-C. acknowledges funding from the Bavarian Hightech Agenda, Germany within the EQAP project and the Deutsche Forschungsgemeinschaft under grant number EXC 2089/1 - 390776260 (Germany's Excellence Strategy). K. M.-C. and J. F. D. were supported by the Helmholtz Association (Germany) under contract VH-NG-1317. J. J. acknowledges support from the Deutsche Forschungsgemeinschaft, Germany under grant SFB 917 Nanoswitches.

References

[1] C.-L. Jia, S.-B. Mi, K. Urban, I. Vrejoiu, M. Alexe, D. Hesse, Atomic-scale study of electric dipoles near charged and uncharged domain walls in ferroelectric films, Nature Mater. 7 (2008) 57–61, http://dx.doi.org/10.1038/nmat2080.

[2] K.W. Urban, Studying atomic structures by aberration-corrected transmission electron microscopy, Science 321 (5888) (2008) 506–510, http://dx.doi.org/10.1126/science.1152800, arXiv:http://www.sciencemag.org/content/321/5888/506.full.pdf. URL http://www.sciencemag.org/content/321/5888/506.abstract.

[3] C.T. Nelson, A. Ghosh, M. Oxley, X. Zhang, M. Ziatdinov, I. Takeuchi, S.V. Kalinin, Deep learning ferroelectric polarization distributions from STEM data via with and without atom finding, NPJ Comput. Mater. 7 (149) (2021) http://dx.doi.org/10.1038/s41524-021-00613-6.

[4] H.J. Chang, S.V. Kalinin, A.N. Morozovska, M. Huijben, Y.-H. Chu, P. Yu, R. Ramesh, E.A. Eliseev, G.S. Svechnikov, S.J. Pennycook, A.Y. Borisevich, Atomically resolved mapping of polarization and electric fields across ferroelectric/oxide interfaces by Z-contrast imaging, Adv. Mater. 23 (21) (2011) 2474–2479, http://dx.doi.org/10.1002/adma.201004641.

[5] T. Denneulin, F. Houdellier, M. Hÿtch, Differential phase-contrast dark-field electron holography for strain mapping, Ultramicroscopy 160 (2016) 98–109, http://dx.doi.org/10.1016/j.ultramic.2015.10.002, URL https://www.sciencedirect.com/science/article/pii/S0304399115300413.

[6] K. Moore, U. Bangert, M.A. Conroy, Aberration corrected STEM techniques to investigate polarization in ferroelectric domain walls and vortices, APL Mater. 9 (2021) 020703.

[7] A. Strauch, B. März, T. Denneulin, M. Cattaneo, A. Rosenauer, K. Müller-Caspary, Systematic errors of electric field measurements in ferroelectrics by unit cell averaged momentum transfers in STEM, Microsc. Microanal. (2023) http://dx.doi.org/10.1093/micmic/ozad016, arXiv:https://academic.oup.com/mam/advance-article-pdf/doi/10.1093/micmic/ozad016/49318970/ozad016.pdf.

[8] L. Yang, K. Dayal, Influence of strain on space-charge distribution at ferroelectric thin-film free surfaces, Acta Mater. 60 (19) (2012) 6457–6463, http://dx.doi.org/10.1016/j.actamat.2012.07.050, URL https://www.sciencedirect.com/science/article/pii/S1359645412004983.

[9] A.C. Twitchett, R.E. Dunin-Borkowski, R.J. Hallifax, R.F. Broom, P.A. Midgley, Off-axis electron holography of electrostatic potentials in unbiased and reverse biased focused ion beam milled semiconductor devices, J. Microsc. 214 (3) (2004) 287–296, http://dx.doi.org/10.1111/j.0022-2720.2004.01328.x, arXiv:https://onlinelibrary.wiley.com/doi/pdf/10.1111/j.0022-2720.2004.01328.x. URL https://onlinelibrary.wiley.com/doi/abs/10.1111/j.0022-2720.2004.01328.x.

[10] D. Gabor, A new microscopic principle, Nature 161 (6) (1948) 777–778, http://dx.doi.org/10.1038/161777a0.

[11] G. Möllenstedt, H. Wahl, Elektronenholographie und rekonstruktion mit laserlicht, Naturwissenschaften 55 (7) (1968) 340–341, http://dx.doi.org/10.1007/BF00600454.

[12] K. Müller, F.F. Krause, A. Beche, M. Schowalter, V. Galioit, S. Löffler, J. Verbeeck, J. Zweck, P. Schattschneider, A. Rosenauer, Atomic electric fields revealed by a quantum mechanical approach to electron picodiffraction, Nature Comm. 5 (2014) 5653:1–8, http://dx.doi.org/10.1038/ncomms6653.

[13] K. Müller-Caspary, F.F. Krause, T. Grieb, S. Löffler, M. Schowalter, A. Béché, V. Galioit, D. Marquardt, J. Zweck, P. Schattschneider, J. Verbeeck, A. Rosenauer, Measurement of atomic electric fields and charge densities from average momentum transfers using scanning transmission electron microscopy, Ultramicroscopy 178 (2017) 62–80, http://dx.doi.org/10.1016/j.ultramic.2016.05.004, URL http://www.sciencedirect.com/science/article/pii/S0304399116300596.

[14] F. Winkler, J. Barthel, R.E. Dunin-Borkowski, K. Müller-Caspary, Direct measurement of electrostatic potentials at the atomic scale: A conceptual comparison between electron holography and scanning transmission electron microscopy, Ultramicroscopy 210 (2020) 112926, http://dx.doi.org/10.1016/j.ultramic.2019.112926, URL http://www.sciencedirect.com/science/article/pii/S0304399119303092.

[15] COMSOLAB, Stockholm, Sweden, COMSOL multiphysics v. 5.5, 2019, URL www.comsol.com.

[16] A.H. Tavabi, V. Migunov, C. Dwyer, R.E. Dunin-Borkowski, G. Pozzi, Tunable caustic phenomena in electron wavefields, Ultramicroscopy 157 (2015) 57–64, http://dx.doi.org/10.1016/j.ultramic.2015.04.003, URL https://www.sciencedirect.com/science/article/pii/S030439911500073X.

[17] M.W. Tate, P. Purohit, D. Chamberlain, K.X. Nguyen, R. Hovden, C.S. Chang, P. Deb, E. Turgut, J.T. Heron, D.G. Schlom, D.C. Ralph, G.D. Fuchs, K.S. Shanks, H.T. Philipp, D.A. Muller, S.M. Gruner, High dynamic range pixel array detector for scanning transmission electron microscopy, Microsc. Microanal. 22 (2016) 237–249, http://dx.doi.org/10.1017/S1431927615015664, URL http://journals.cambridge.org/article_S1431927615015664.

[18] G. Moellenstedt, H. Dueker, Beobachtungen und messungen an biprisma-interferenzen mit elektronenwellen, Z. Phys. 145 (1956) 377–397, http://dx.doi.org/10.1007/BF01326780.

[19] H. Lichte, Electron holography approaching atomic resolution, Ultramicroscopy 20 (3) (1986) 293–304, http://dx.doi.org/10.1016/0304-3991(86)90193-2, URL http://www.sciencedirect.com/science/article/pii/0304399186901932.

[20] M. Beleggia, T. Kasama, R.E. Dunin-Borkowski, S. Hofmann, G. Pozzi, Direct measurement of the charge distribution along a biased carbon nanotube bundle using electron holography, Appl. Phys. Lett. 98 (24) (2011) http://dx.doi.org/10.1063/1.3598468, arXiv:https://pubs.aip.org/aip/apl/article-pdf/doi/10.1063/1.3598468/9391586/243101_1_online.pdf.

[21] J.M. Cowley, A.F. Moodie, The scattering of electrons by atoms and crystals. I. A new theoretical approach, Acta Crystallogr. 10 (10) (1957) 609–619, http://dx.doi.org/10.1107/S0365110X57002194.

[22] G. Matteucci, G.F. Missiroli, G. Pozzi, Simulations of electron holograms of long range electrostatic field, Scanning Microsc. 11 (1997) 367–374.

[23] M. Vulovic, L.M. Voortman, L.J. van Vliet, B. Rieger, When to use the projection assumption and the weak-phase object approximation in phase contrast cryo-EM, Ultramicroscopy 136 (2014) 61–66.

[24] K. Harada, Interference and interferometry in electron holography, Microscopy 70 (1) (2020) 3–16, http://dx.doi.org/10.1093/jmicro/dfaa033, arXiv:https://academic.oup.com/jmicro/article-pdf/70/1/3/36194500/dfaa033.pdf.

[25] T. Tanigaki, Y. Inada, S. Aizawa, T. Suzuki, H.S. Park, T. Matsuda, A. Taniyama, D. Shindo, A. Tonomura, Split-illumination electron holography, Appl. Phys. Lett. 101 (4) (2012) 043101, http://dx.doi.org/10.1063/1.4737152, URL http://link.aip.org/link/?APL/101/043101/1.

[26] K. Harada, H. Kasai, Accumulated reconstruction method for electron holography, Microsc. Microanal. 20 (S3) (2014) 248–249, http://dx.doi.org/10.1017/S1431927614002967, arXiv:https://academic.oup.com/mam/article-pdf/20/S3/248/48284623/mam0248.pdf.

[27] L. Kou, J. Chen, Eliminating the influence of the perturbed reference wave in electron holography, J. Modern Opt. 42 (1995) 1171–1178, http://dx.doi.org/10.1080/09500349514551021.

[28] M. Beleggia, T. Kasama, D.J. Larson, T.F. Kelly, R.E. Dunin-Borkowski, G. Pozzi, Towards quantitative off-axis electron holographic mapping of the electric field around the tip of a sharp biased metallic needle, J. Appl. Phys. 116 (2) (2014) 024305, http://dx.doi.org/10.1063/1.4887448.

[29] F. Zheng, J. Caron, V. Migunov, M. Beleggia, G. Pozzi, R.E. Dunin-Borkowski, Measurement of charge density in nanoscale materials using off-axis electron holography, J. Electron Spectrosc. Relat. Phenom. 241 (2020) 146881, http://dx.doi.org/10.1016/j.elspec.2019.07.002, Sources, Interaction with Matter, Detection and Analysis of Low Energy Electrons (SIMDALEE2). URL https://www.sciencedirect.com/science/article/pii/S0368204818302032.

[30] J. Zweck, F. Schwarzhuber, J. Wild, V. Galioit, On detector linearity and precision of beam shift detection for quantitative differential phase contrast applications, Ultramicroscopy 168 (2016) 53–64, http://dx.doi.org/10.1016/j.ultramic.2016.05.007, URL http://www.sciencedirect.com/science/article/pii/S0304399116300699.

[31] J. Verbeeck, A. Béché, K. Müller-Caspary, G. Guzzinati, M.A. Luong, M. Den Hertog, Demonstration of a 2x2 programmable phase plate for electrons, Ultramicroscopy 190 (2018) 58–65, http://dx.doi.org/10.1016/j.ultramic.2018.03.017.